WILEY | Hindawi

Research Article

Quantitative Visualization Monitoring of Cracks at Shotcrete-Rock Interface Based on Acoustic Emission

Yuzhu Guo,[1] Xudong Chen [ID],[2] Jin Wu,[2] Tao Ji,[3] and Yingjie Ning [ID][4]

[1]*School of Civil Engineering, Changsha University of Science & Technology, Changsha 410114, China*
[2]*College of Civil and Transportation Engineering, Hohai University, Nanjing 210098, China*
[3]*Department of Civil Engineering, Fuzhou University, Fuzhou 350116, China*
[4]*Zhejiang Communications Construction Group Co., Ltd., Hangzhou 310051, China*

Correspondence should be addressed to Xudong Chen; cxdong1985@hotmail.com

To investigate the possibility of quantitative monitoring of the fracture process zone (FPZ) at the shotcrete-rock interface, the acoustic emission (AE) and digital image correlation (DIC) are used to monitor the three-point bending test of shotcrete-rock specimens. Firstly, the AE intensity signal characteristics during damage to the shotcrete-rock interface are analyzed. Then, the spatial *b*-value of AE is used to visually characterize the shotcrete-rock interface damage, and the interface damage characteristics of two specimens, shotcrete-granite and shotcrete-sandstone, are analyzed using this analysis method. The analysis reveals that not only the AE spatial *b*-value can determine the location of microdamage within the interface but it can also characterize the degree of damage. Finally, a new parameter, *Tb*-value, is constructed based on the AE spatial *b*-value to quantitatively characterize the FPZ, and the newly established characterization method is validated with the FPZ monitored by DIC. The results show that the *Tb*-value not only locates and visually characterizes the location of the FPZ within the specimen but also enables the quantitative determination of the FPZ. This provides a new idea for localizing and quantitatively monitoring cracks and FPZs inside structures using AE techniques.

1. Introduction

Many tunnels have been built in central and western China, some of which are deep and cut through earthquake zones. The deep underground tunnel will deform and collapse under the disturbance of external forces such as ground stress and geological disaster [1]. Accident investigation shows that many engineering disasters are related to interface damage [2]. Thus, the fracture characteristics of the shotcrete-rock interface under various stress fields have been investigated, making useful progress in understanding fracture toughness [3], energy release rate, and cracking modes [4]. It has also been shown that the interfacial roughness, cohesion, and aggregate occlusion affect the interface's fracture characteristics [5, 6]. Based on experimental results, scholars have summarized the theoretical criterion of interface fracture from different perspectives, namely, pressure theory [7], energy theory [8], and stress intensity factor theory [9].

However, most analyses of fracture properties for the concrete-rock interface have relied on linear elastic fracture mechanics (LEFM) [10, 11]. The shotcrete-rock interface is made up of quasi-brittle material, and the presence of the fracture process zone (FPZ) leads to changes in the stress field at the crack tip, which can significantly affect the interface's fracture behavior and path [12]. Therefore, it is essential to study the characteristics of the FPZ at the shotcrete-rock interface to better understand its nonlinear fracture properties. Currently, the FPZ of single materials has been studied more frequently, and the dimensional evolution characteristics of the FPZ in concrete are supported by relevant theoretical explanations [13, 14]. Various studies on the FPZ of concrete or rock show mutual corroboration [15–17], and the DIC technique is critical in measuring the FPZ. Many successful studies have utilized the DIC technique to characterize fracture evolution on material surfaces [18–21], and its accuracy is adequate for measuring the FPZ [22, 23]. Studies by Moazzami

et al. [24] on barite and sandstone separately found that the length of the FPZ was related not only to material type and size but also to fracture mode, with the length increasing when the loading mode changed from type I to type II. Zhang et al. [25] studied the size effect of the FPZ of rocks and found that the length and width of the FPZ increased with specimen size, and the specimen's thickness had a significant effect on the width of the FPZ. With accumulated experimental experience, recent studies on single materials have developed numerical models that account for FPZ effects [26–29]. However, in the case of the shotcrete-rock interface, the evolutionary characteristics of the FPZ are jointly influenced by the materials on both sides of the interface, which differ from those of a single material. Dong et al. [9, 22] conducted substantial experimental and theoretical work on the FPZ at the concrete-rock interface. They summarized the evolution characteristics of the FPZ under different fracture modes and proposed a numerical method for the crack extension at the shotcrete-rock interface. Monitoring the shotcrete-rock interface structures using DIC techniques and equipment is difficult due to deep submergence and the internal extension of cracks. AE techniques have been widely used in material damage evaluation [30, 31], can monitor underwater, locate microdamage inside the material, and become a feasible way to quantify the FPZ. However, to the authors' knowledge, no studies have reported on measuring the FPZ at the shotcrete-rock interface using AE techniques.

The aim of this study is to investigate the influence of rock type on the FPZ of the shotcrete-rock interface. Initially, the DIC technique was used to analyze the evolutionary characteristics of the FPZ of shotcrete-rock specimens subjected to three-point bending loads. Then, based on the AE spatial b-value damage visualization characterization method, a new parameter, Tb-value, was constructed to quantitatively characterize the FPZ, and the newly established characterization method was validated using the FPZ monitored by DIC. The results demonstrate that the Tb-value parameter not only locates and visually characterizes the location of the FPZ within the specimen but also enables quantitative determination of the FPZ. This provides a new idea for localizing and quantitatively monitoring cracks and FPZs inside structures using AE techniques.

2. Experimental Program

2.1. Specimen Preparation. The cementitious material used in this experiment was P·O 42.5 Portland cement, with river sand (fineness modulus 2.6) as the fine aggregate and basalt gravel (particle size 5–10 mm) as the coarse aggregate. Laboratory tap water was used, along with a high-performance polycarboxylic acid water reducer. The mix proportions are presented in Table 1.

Each shotcrete-rock specimen prepared for this test measured 100 mm × 100 mm × 400 mm, with a crack height ratio of 0.3 at the interface prenotch. A mutually perpendicular grid interface was created by cutting horizontal and vertical groove lines at the rock interface, with a groove line width and depth of 5 mm. The spacing of the slot lines can form a grid interface with different roughness levels. In this

TABLE 1: Mix proportion of concrete specimens (kg/m^3).

Cement	Fine aggregate	Coarse aggregate	Water	Water reducer
450	971	795	180	2.25

experiment, three interfaces with different roughness levels (B, C, and D) were produced by using slot line spacing of 35 mm, 21 mm, and 15 mm, respectively. The 3D scanning schematic of the interface is shown in Figure 1. Shotcrete-granite specimens were made with granite having three interface roughness levels (B, C, and D). Additionally, shotcrete-sandstone specimens with an interfacial roughness of D were made to compare the effect of rock type on interfacial fracture damage. The compressive strengths of granite, sandstone, and shotcrete are 154.50 MPa, 49.07 MPa, and 54.67 MPa, respectively. Table 2 presents the basic information of the shotcrete-rock specimens used in the experiment.

2.2. Test Setup. The closed-loop servo-controlled material testing system (MTS 322) with a capacity of 500 kN was used to perform tests on the specimens. A clip extensometer installed at the prenotch mouth at the bottom of the specimen controlled the load application rate, with the crack mouth opening displacement (CMOD) rate set at 0.001 mm/s. Each roughness of the specimens underwent three sets of loading tests. The data acquisition system for acoustic emission used the all-weather structural health monitoring system manufactured by MISTRAS, USA, with a model number Sensor Highway III. Six PK6I AE sensors with a built-in 26 dB low-power amplifier were placed on the surface of the specimen, and the AE signal acquisition threshold was set at 40 dB. The peak definition time (PDT), the hit definition time (HDT), and the hit lockout time (HLT) were set to 50, 150, and 300 μs, respectively. The 3D DIC data acquisition system used ARAMIS Professional, produced by GOM, Germany. Two high-speed cameras with a model number ARAMIS Adjustable Base captured digital images. To meet the shooting measurement requirements of the DIC software system, white primer and black random scattering spots were sprayed on the span-center region of the specimen using matte spray paint. The location of the AE sensors and scattering areas are shown in Figure 2.

3. Methodology

3.1. Intensity Signal Analysis Method. Intensity signal analysis (ISA) is a technique for evaluating damage characteristics based on AE signal intensity. The signal intensity can be correlated with the integral of the rectified voltage signal over the duration of the AE signal and is an effective means of assessing the degree of damage within materials [32]. The method has two parameters: the history index (HI) and the severity index (S_r). HI characterizes the slope of the cumulative signal intensity over time by comparing the signal intensity of all hits, which can be obtained by the following equation [33]:
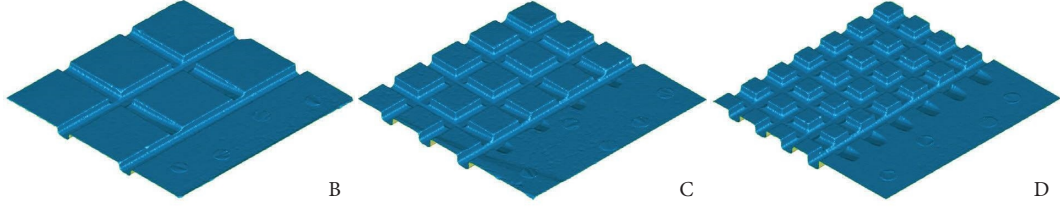
Figure 1: 3D scanning diagram of rock interface.

Table 2: Basic information of shotcrete-rock specimens.

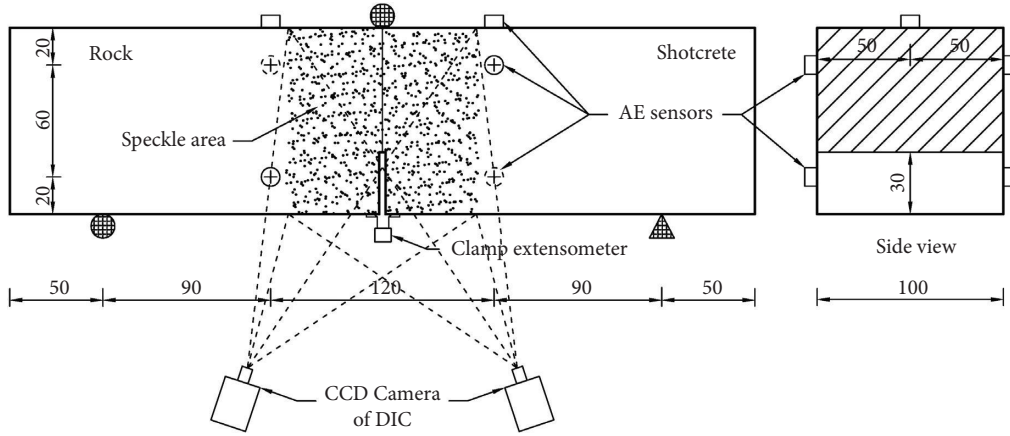| Specimens	Interface roughness levels	Rock types	Strength of concrete (MPa)
HB	B	Granite	54.67
HC	C	Granite	54.67
HD	D	Granite	54.67
SD	D	Sandstone	54.67

Figure 2: Schematic diagram of AE sensors position and speckle area (unit: mm).

$$HI(t) = \frac{N_{hit}}{N_{hit} - K}\left(\frac{\sum_{i=K+1}^{N} S_{oi}}{\sum_{i=1}^{N} S_{oi}}\right), \quad (1)$$

where HI (t) is the historical index at moment t; N_{hit} is the number of hits up to moment t; S_{oi} is the signal intensity of the ith hit; K is an empirical constant, and the K-parameter of rock and concrete materials is defined in Table 3.

The severity index can be calculated by the following equation [34]:

$$S_r = \frac{1}{J}\left(\sum_{i=1}^{J} S_{om}\right), \quad (2)$$

where S_r is the severity index; S_{om} is the signal intensity of the mth hit; J is an empirical constant; and the J-parameter of rock and concrete materials is defined in Table 4.

Table 3: K-parameter of rock and concrete materials [34].

Hits	≤50	51–200	201–500	≥501
K	—	$N_{hit} - 30$	$0.85N_{hit}$	$N_{hit} - 75$

Table 4: J-parameter of rock and concrete materials.

Hits	< 50	≥51
J	—	50

3.2. Spatial b-Value Analysis Method. The b-value is a term used in seismology to describe the magnitude-frequency relationship of earthquakes. The magnitude is linearly related to the logarithm of the cumulative frequency, with its slope referred to as the b-value [35]. This b-value relationship also exists for the amplitude-cumulative frequency of AE. There is a close connection between the AE b-value and the development of microcracks inside the material in response to the applied load. As the b-value decreases, the microcracks within the material develop into macroscopic cracks [36]. Spatial b-values are utilized in seismic activity studies to determine anomalous activity at fault locations in seismic fault zones [37]. To assess the relationship between damage at the shotcrete-rock interface and the AE b-value, a 100×120 mm grid model was established within the span of the shotcrete-rock specimens.

The spatial b-value of AE was calculated based on spatial coordinate information of AE events from the fracture damage process at the shotcrete-rock interface. The schematic diagram of the grid point array used for calculating the spatial b-value is shown in Figure 3, with the location of the 100×120 mm grid area being the region between the AE sensors in Figure 2. The calculation flow is demonstrated in Figure 4, with key details described as follows:

(a) Datum points for calculating spatial b-value spaced at L intervals within a 100×120 mm area in the span of the shotcrete-rock specimen were generated.

(b) The initial cylinder that picks up AE event data has the datum points as the center of the circle, r as the radius, and H as the height. The threshold value of the number of AE events required to calculate the spatial b-value is set to N. r increases based on the pickup threshold until the number of AE events picked up within the cylinder range meets the threshold requirement. H can be adjusted by balancing the total number of AE events and the program's computational efficiency. The maximum value of r is set to R to prevent nonconvergence of r at the edge position.

(c) The Aki method is used to calculate the spatial b-value with the following equation [38]:

$$b = \frac{20 \log_{10} e}{a - a_c}, \tag{3}$$

where a is the average amplitude; a_c is the threshold amplitude, the threshold amplitude set for this test is 40 dB; e is the Euler number.

(d) If a b-value of 0 occurs at an individual location, the b-value of that point is replaced with the average of its neighboring benchmark points. Lastly, a heat map displaying the spatial b-value matrix is created for visual representation.

3.3. Digital Image Correlation Analysis Method. DIC can accomplish measuring the surface deformation of an object without contact, unlike traditional testing methods. During the three-point bending loading process, local deformation on the shotcrete-rock specimen surface leads to changes in the deformation of black random scattered spots and relative positioning. The high-speed camera of the DIC system records this change in the local strain or displacement field, allowing for accurate surface measurement of the displacement or strain field by comparing changes in the black scattered spots' digital image across various loading stages. Once the surface displacement field has been determined, crack size measurements are made possible. The modeling of crack extension measurement is depicted in Figure 5. Since crack extensions zigzag upward rather than strictly vertically, determining crack width by directly approaching the crack edge presents a challenge. Equidistant points are chosen to establish a pair of vertical directions within a narrow width on both sides of the crack trajectory, with their connecting lines forming horizontal line segments such
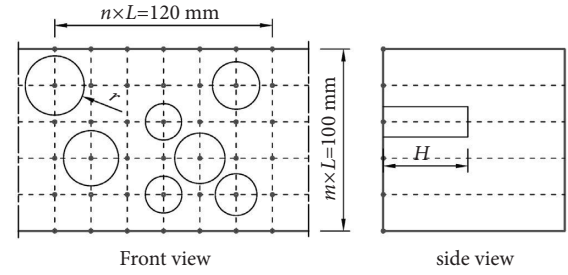

FIGURE 3: Schematic diagram of grid lattice.

as U_1V_1, U_2V_2, ..., U_nV_n. Then, the horizontal displacement on each line segment is extracted. When the crack forms, the horizontal displacement curve will have a turning point, as shown in Figure 6, and the distance between these turning points represents the crack width. Therefore, DIC can monitor the opening displacement at any height on the surface of shotcrete-rock specimens, allowing for the characterization of the evolutionary features of the FPZ.

4. Results and Discussion

4.1. AE Intensity Signal Analysis. To analyze the signal intensity characteristics of acoustic emission (AE) at different loading stages, AE signal intensity indices of shotcrete-rock specimens are compared with corresponding load-time curves as shown in Figure 7. At the start of loading, lg (S_r) for all four specimens is at a low level and increased rapidly with increasing load. In Figures 7(a)–7(c), lg (S_r) for granite reached a high level when the loading curve entered the nonlinear section and remained high during peak and postpeak loading. In contrast, lg (S_r) for the fourth specimen continued to grow after the load curve entered the nonlinear phase until it peaked at $0.2F_{\max}$ after which it remained at its highest value for the residual phase of the load. This indicates that lg (S_r) is more sensitive to damage in brittle shotcrete-granite specimens, reaching high values just before peak load. Roughness increased slightly with peak values of lg (S_r), which are 6.74, 7.12, and 7.16 for B, C, and D roughness specimens, respectively. For shotcrete-sandstone specimens, since the strength and elastic modulus of sandstone are less than those of shotcrete, fracture occurred on the sandstone side. Therefore, sandstone's plastic damage prevented lg (S_r) from reaching an extreme value before reaching the destabilizing load. Once the load profile hits the destabilizing load, macroscopic crack expansion dominated, and severe damage caused lg (S_r) to increase again. HI curves in Figures 7(a)–7(d) showed that HI is more sensitive to transient damage, exhibiting extremely sharp peaks at the moment of sudden brittle cracking. For the four types of shotcrete-rock specimens, significant fluctuations in the instantaneous HI mostly occur after reaching the destabilizing load, signifying the progression of damage.

The HI and lg (S_r) parameters reveal the damage characteristics of shotcrete-rock specimens during three-point bending fracture, each reflecting its own set of features. Hence, the correlation between these two parameters is significantly linked to damage properties across the
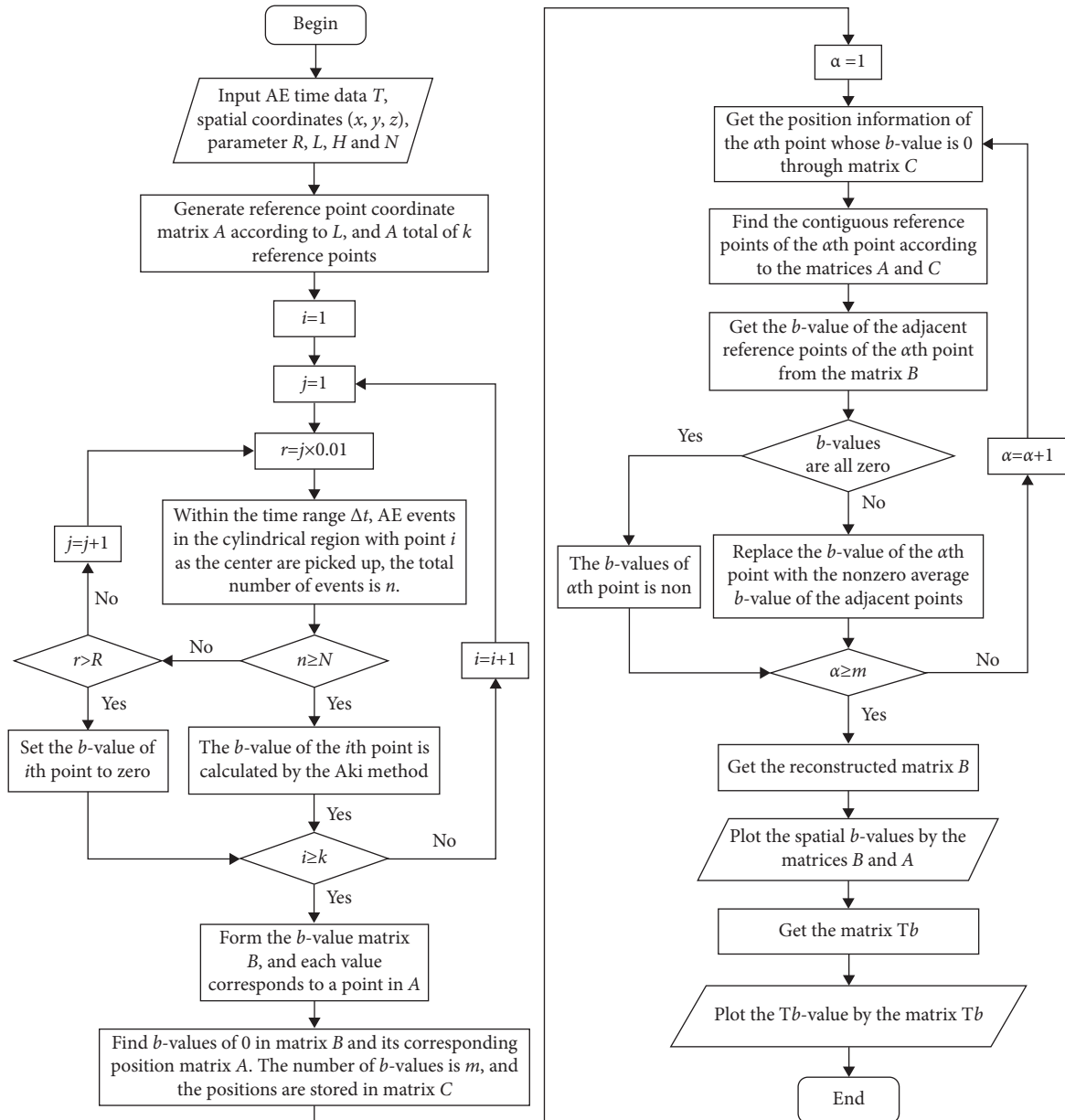
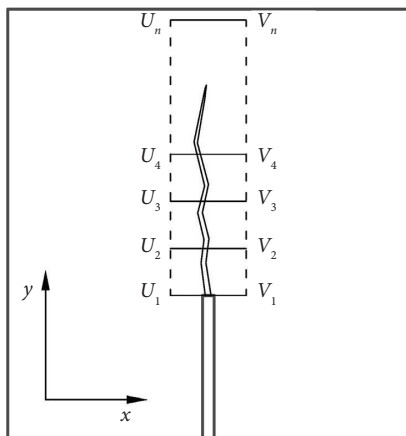FIGURE 4: Flowchart of calculation of spatial *b*-value.

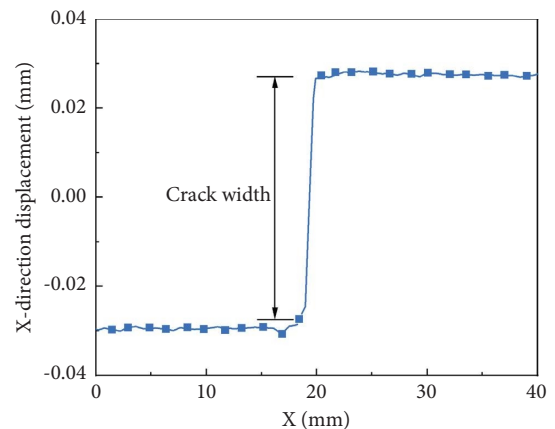FIGURE 5: Calculation diagram of crack width.

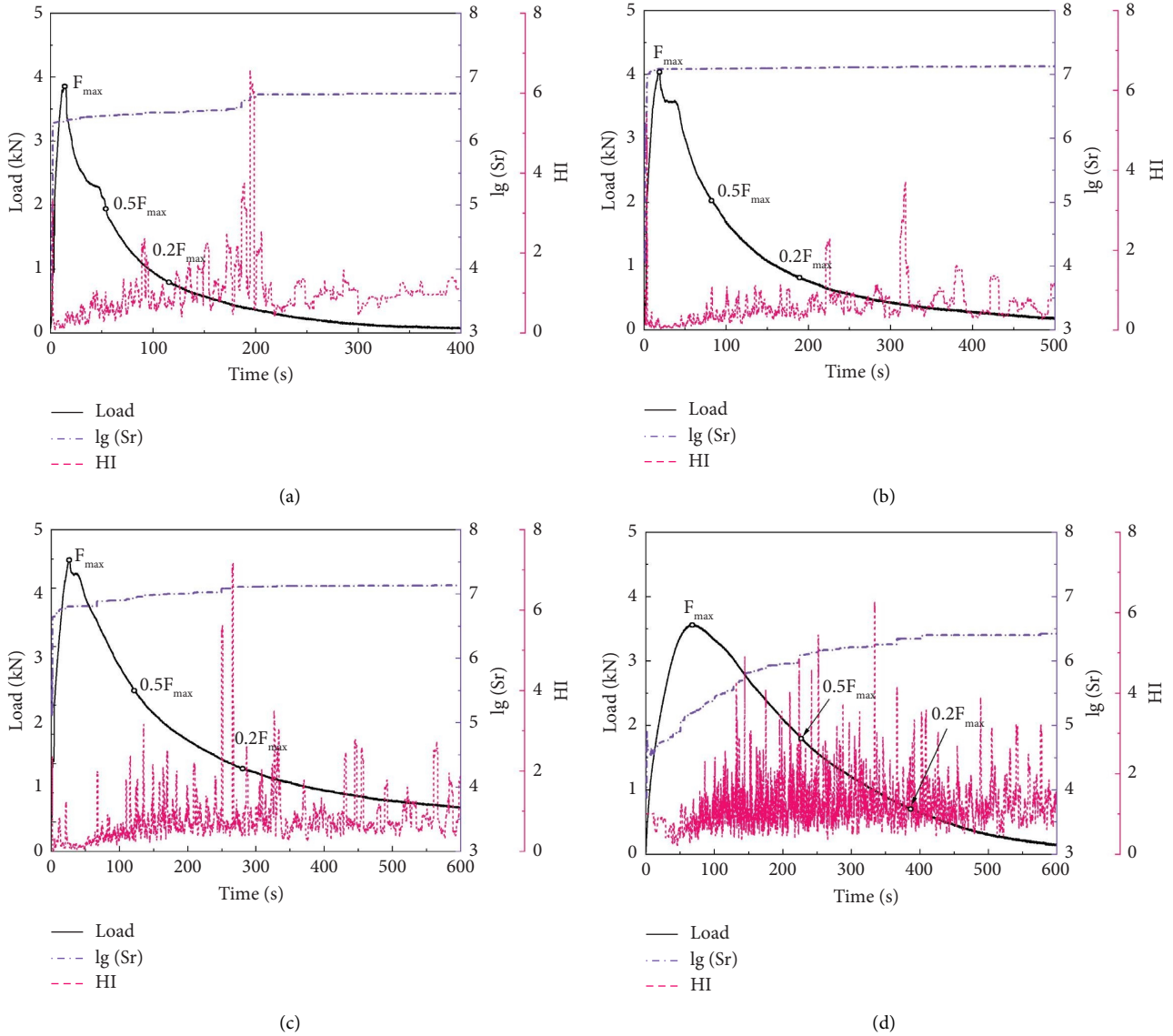FIGURE 6: Schematic diagram of crack width.

FIGURE 7: Signal intensity index characteristics of shotcrete-rock specimen. (a) Specimen HB. (b) Specimen HC. (c) Specimen HD. (d) Specimen SD.

different loading stages. Based on the load curve characteristics, the loading stages are divided into four segments: $0 \sim F_{max}$, $F_{max} \sim 0.5F_{max}$, $0.5F_{max} \sim 0.2F_{max}$, and $0.2F_{max} \sim$, and the results are illustrated in Figure 8. Analysis indicates that the HI-lg (S_r) relationship experiences greater fluctuations during the initial stage from 0 to F_{max}, primarily due to the brittleness of granite. This causes the history index-log severity index relationship of shotcrete-granite specimens to almost reach the maximum range of both values at this point. However, there is lesser fluctuation in the subsequent three stages, devoid of any obvious phasing characteristics. Conversely, shotcrete-sandstone specimens portray apparent phasing characteristics in all four loading stages, making it easier to determine the loading stages of the loads, similar to the phasing characteristics of three-point bending fracture of pure concrete materials [32].

4.2. Analysis of FPZ. The FPZ is considered as the fracturing region with partial cohesion, and the demarcation point between the FPZ and the macroscopic fracture is defined as the critical fracture opening displacement (w_0). To calculate the w_0, the empirical equation $w_0 = 6G_f/f_t$ is used here with reference to the study of Dong et al. [5]. Furthermore, the fracture energy is calculated using the empirical formula from the literature [39]. The specific results of w_0 are displayed in Table 5. Ten typical loading stages, as shown in Figure 9, are chosen to analyze the crack width of each shotcrete-rock specimen after determining w_0. The length of the FPZ is schematized according to w_0, and the findings are presented in Figure 10.

From Figures 10(a) to 10(c), it is apparent that as roughness increases, crack width increases for shotcrete-granite specimens with varying roughness interfaces at the
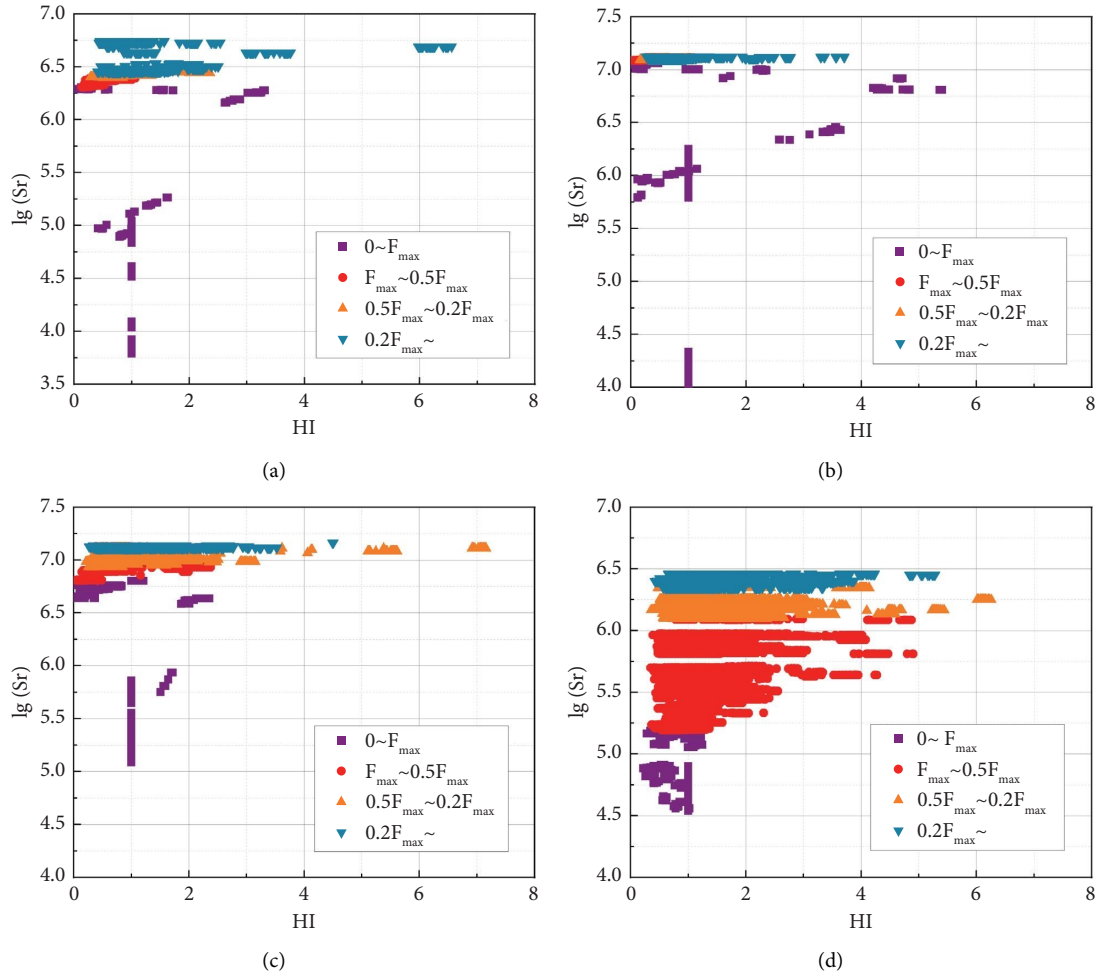
(a)

(b)

(c)

(d)

FIGURE 8: Signal intensity index of shotcrete-rock specimen at different loading stages. (a) Specimen HB. (b) Specimen HC. (c) Specimen HD. (d) Specimen SD.

TABLE 5: Calculation results of critical crack opening displacement.

Specimen	f_t (MPa)	G_f (N/m)	w_0 (mm)
HB	2.11	35.48	0.132
HC	2.70	53.98	0.153
HD	2.92	84.12	0.173
SD	2.26	95.59	0.254

same loading stage. The residual bond stress at the rough interface is higher for the same crack width due to the shotcrete aggregate and rock interface's tectonic joints playing a more pronounced occlusal role postcracking as roughness rises. When specimens with different roughness achieve the same load level, larger interfacial roughness specimens have significantly greater crack widths. When the crack width exceeds w_0, the crack is in a stress-free state, and the end of the FPZ begins to rise. From Figures 10(a)–10(c), it is apparent that when loaded to postpeak $0.1F_{\max}$, the CTOD of the prenotch of the HB specimen does not reach the critical value, and the FPZ tips of HC and HD rose, respectively, to 45.3 mm and 52.7 mm of the specimen height, while the different roughness specimens' FPZ tips at
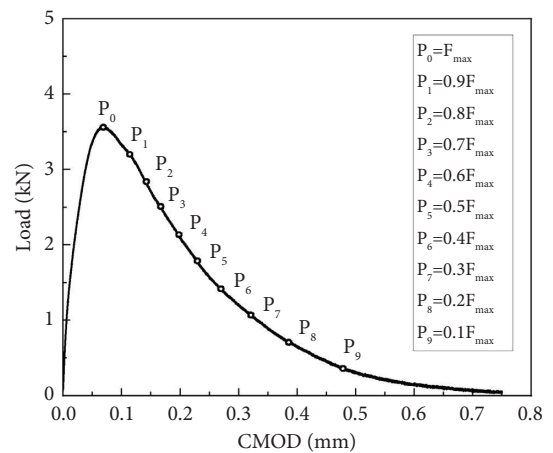

FIGURE 9: Schematic diagram of typical loading stage.

this loading stage had differing positions and were slightly lower as roughness increased. Comparing Figures 10(a) and 10(d), the CTOD at both specimens almost reaches their respective critical values when loaded to slightly above
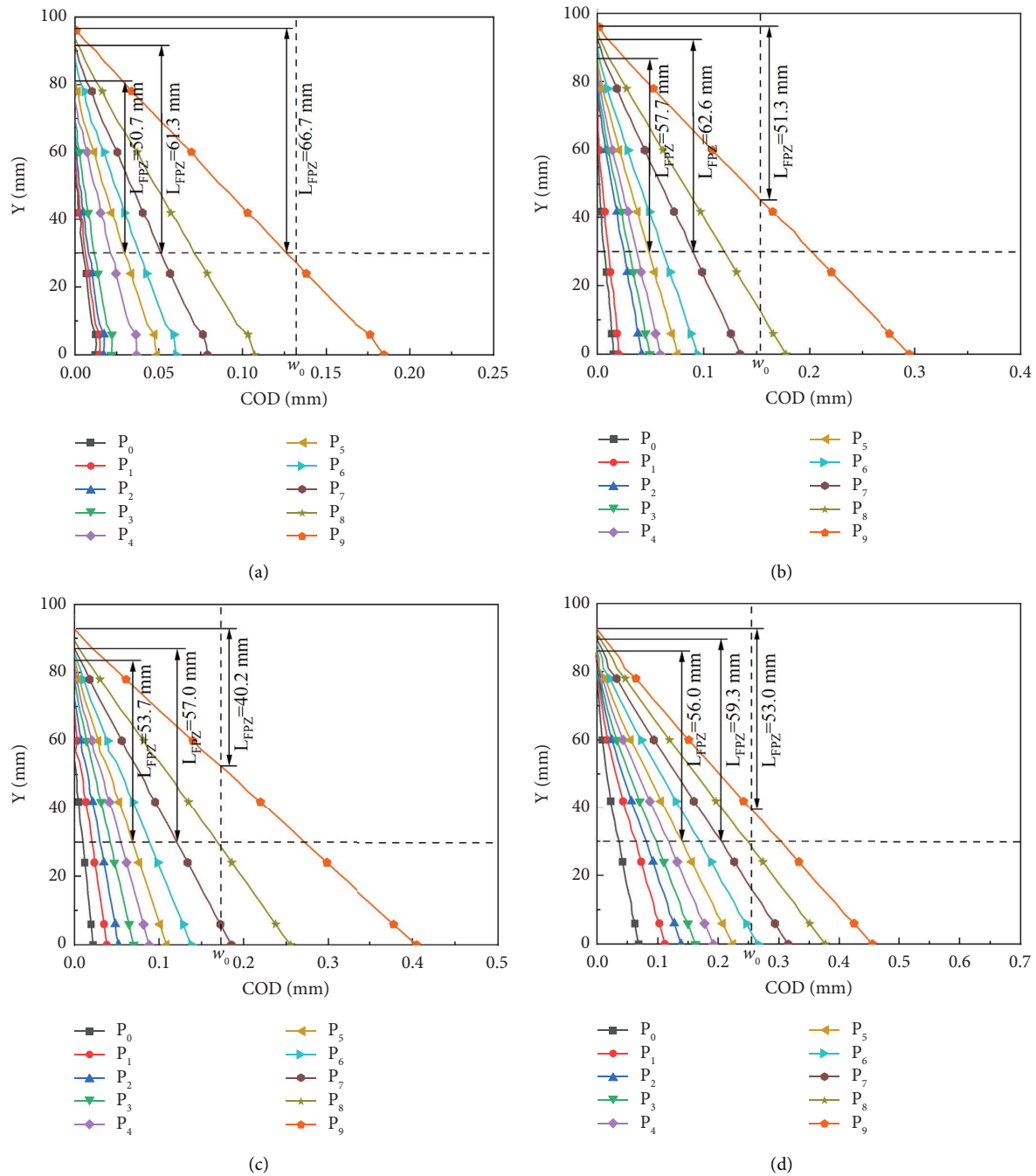
FIGURE 10: Schematic diagram of crack width in specimen height direction at different loading stages. (a) Specimen HB. (b) Specimen HC. (c) Specimen HD. (d) Specimen SD.

postpeak $0.2F_{max}$, although their rock types differ and the length of the FPZ in the shotcrete-sandstone specimen is somewhat longer than that in the shotcrete-granite specimen. To quantitatively compare the development of FPZ in different specimens, the length variations of FPZ with crack extension were calculated for four shotcrete-rock specimen types, as shown in Figure 11. The horizontal axis in Figure 11 represents the ratio of effective crack length to specimen height minus prenotch depth. Results show that FPZ develops similarly across different specimens regardless of

their roughness and rock type. As the fracture expands, FPZ length continues to grow until it reaches its maximum peak. The peak FPZ lengths are 66.8 mm for both HB and HC specimens, 59.7 mm for HD, and 62.3 mm for SD, with corresponding percentages of effective fractures of 0.95, 0.95, 0.85, and 0.89, respectively. Subsequently, the length of the unstressed crack increases while the length of the FPZ decreases rapidly. The rapid reduction of the FPZ is attributed to the boundary effect of the specimen, as observed in Figure 10, where the expansion rate decreases significantly
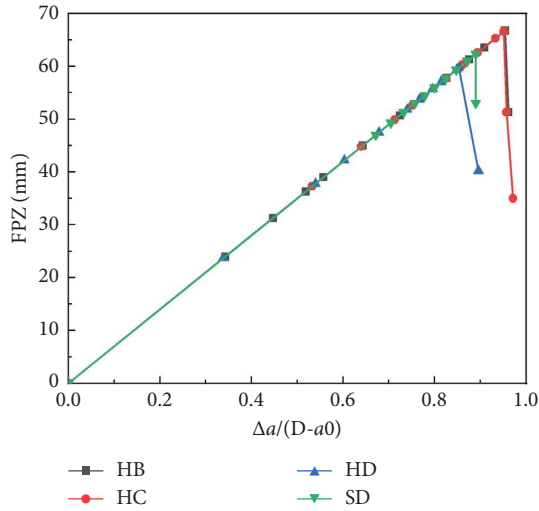
FIGURE 11: Comparison of the length of the fracture process zone.

FIGURE 12: Fracture morphology of HD and SD specimens.

near the specimen's boundary. Additionally, stress-free cracks are generated at a high rate causing a rapid rise at the end of the FPZ and a consequent decrease in the length of the FPZ.

4.3. AE-Based Damage Visualization Analysis. The crack propagation path in shotcrete-rock materials is dependent on the properties of the materials on both sides of the interface. Due to differences in material characteristics, cracks may propagate along the interface or on the weaker material side. Figure 12 shows typical crack patterns of HD and SD specimens; the crack in shotcrete-granite specimens expands vertically upward along the interface, whereas the crack in shotcrete-sandstone specimens is biased toward the sandstone side due to its lower tensile strength and elastic modulus compared to shotcrete. The loose structure and high porosity of sandstone allow cement slurry to penetrate into it during shotcrete casting at the interface, making it stronger than the sandstone interior. Consequently, cracks are more likely to spread inward rather than along the interface in this case.

Damage processes in shotcrete-rock materials often occur in weak areas but not exclusively at cracks. For interfaces of different rock types, whose internal damage characteristics are unknown, DIC techniques effectively monitor surface deformation and cracking. AE techniques detect elastic wave signals released during material damage and localize the signal source, albeit characterizing the AE source as discrete points without enabling the determination of the degree of damage at various locations inside the interface. The AE spatial b-value can provide information about damage sites inside the material, while its magnitude can reflect the degree of local damage within the material. Calculation parameters must be defined, and N is typically set to 50 to attain stable b-value calculation results [40]. Other running parameters are determined based on factors such as data volume, computational efficiency, and image resolution. Testing revealed that R, L, and H settings of

15 mm, 1 mm, and 100 mm are appropriate for granite, and 8 mm, 1 mm, and 50 mm for sandstone. The incremental gradient of r is set at 0.01 mm in accordance with the accuracy of AE signal acquisition during testing. Using these parameters, the spatial b-values of HD and SD specimens are calculated. Schematic diagrams of the spatial b-values of HD and SD specimens are generated for different loading stages, illustrated in Figures 13 and 14.

Figure 12 shows that the shotcrete-granite specimen consists of concrete on the left and granite on the right. Figure 13(a) reveals that when this specimen is loaded to the P_3 stage, the damage has already occurred throughout almost the entire height range of the interface, and the spatial b-value on the concrete side is significantly smaller than that on the granite side, indicating that the damage on the concrete side is greater at the P_3 stage. As loading continues to the P_5 stage, the development of the FPZ above the prenotch tip persists, causing further accumulation of damage at that location, represented by the small spatial b-value above the prenotch tip in Figure 13(b). With further loading, the FPZ located at the shotcrete-granite interface continues to develop, and damages are concentrated at the interface location. The smallest spatial b-value in the interface region can be seen in Figures 13(c) and 13(d). After loading to stage P_9, the end position of the FPZ shifts upward, and the damage accumulates mainly in the middle-upper part of the specimen cross section. The spatial b-value cloud plot region in Figure 13(e) corresponds to this trend.

As shown in Figure 12, the shotcrete-sandstone specimen is composed of sandstone on the left side and concrete on the right side. Figure 14(a) reveals that when loaded to the P_3 stage, the damage range is distributed within 20 mm on both sides of the interface, implying that the microdamage depth ranges on either side of it are similar. As the load increases to stage P_5, the FPZ above the prenotch tip continues to develop in the sandstone. The spatial b-value cloud in Figure 14(b) indicates that most of the damaged area shifts to the sandstone side. Subsequent cracks continue to expand in the sandstone, leading the damage to be concentrated in that specific area, and the smallest spatial b-value in the sandstone region is seen in Figures 14(c) and 14(d). Once the load reaches stage P_9, the end position of the FPZ in the sandstone shifts upward. The spatial b-value cloud in Figure 14(e) illustrates that the damage site also moves upwards and away from the prenotch tip, indicating that new damage signals are almost no longer generated at the stress-free fracture site.
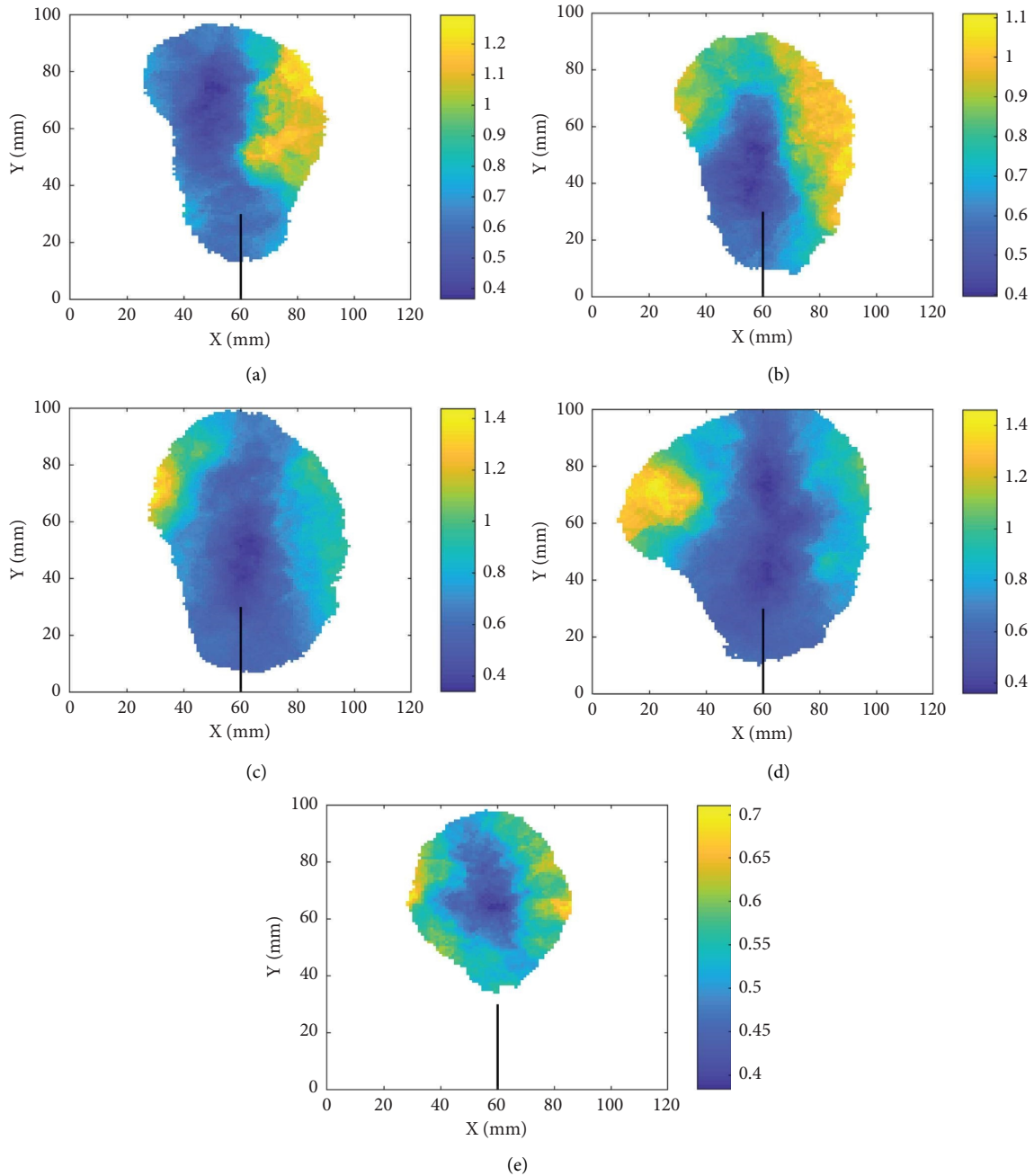
FIGURE 13: Schematic diagram of spatial b-value of HD specimen at different loading stages. (a) $0\sim P_3$ stage. (b) $P_3\sim P_5$ stage. (c) $P_5\sim P_7$ stage. (d) $P_7\sim P_9$ stage. (e) $P_9\sim$end stage.

4.4. FPZ Analysis Based on Parameter Tb. Damage to shotcrete-rock specimens involves not only the extension of macroscopic cracks but also a significant accumulation of microdamage within the fracture zone area before the formation of macroscopic cracks. Figures 13 and 14 illustrate that processing the AE source data, which contains some marginal areas of minor damage, generates an AE spatial b-value heat map covering the entire damaged area. Further processing of these data is necessary to distinguish severely damaged regions from microdamaged ones and improve the visualization of the damage characteristics. Locations with intense damage typically have more localized AE sources, and localization intensity is positively correlated with the level of damage. When calculating the spatial b-value, R, the parameter for the datum points with dense AE source localization data, should be small. Therefore, the Hadamard product $[T]$ of the spatial b-value matrix $[B]$ and the corresponding radius matrix $[R]$ is calculated first. Next, the resulting $[T]$ matrix is element-normalized by dividing all elements by the maximum element value of this matrix. This process generates the new matrix $[Tb]$, which is calculated as follows:
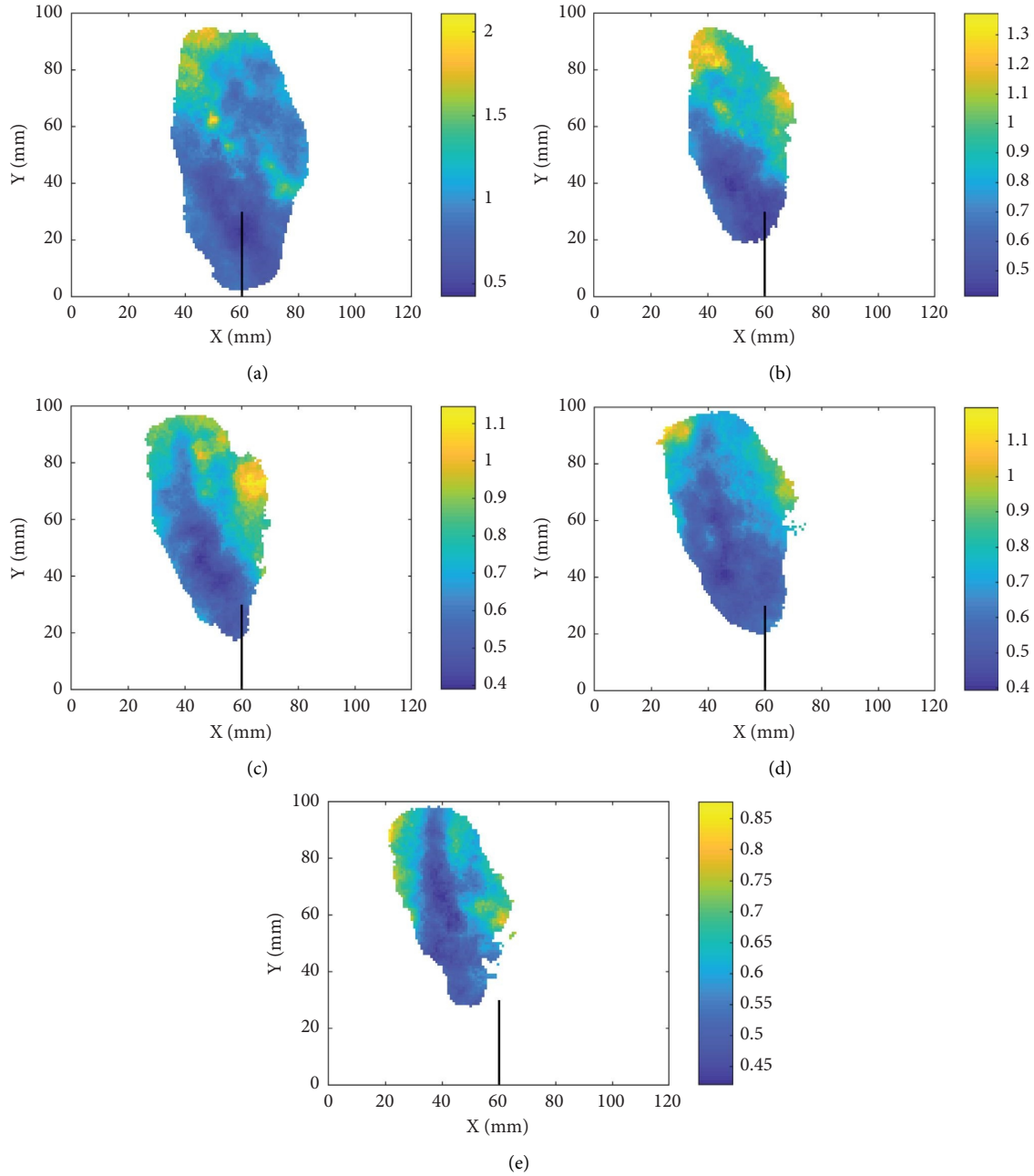
Figure 14: Schematic diagram of spatial *b*-value of SD specimen at different loading stages. (a) $0\sim P_3$ stage. (b) $P_3\sim P_5$ stage. (c) $P_5\sim P_7$ stage. (d) $P_7\sim P_9$ stage. (e) $P_9\sim$end stage.

$$[Tb] = \frac{[T]}{\max[t_{ij}]},$$

$$[T] = [B] \odot [R]. \tag{4}$$

The *Tb* values for the HD and SD specimens are calculated, and the cracks monitored by DIC are set to black in combination with the *Tb* heat map to compare the relative position relationship between the two. The crack morphology is obtained by binarization of digital image postprocessing results. The crack positions and *Tb* heat maps of the HD and SD specimens at different loading stages are plotted separately, and

the comparison results are shown in Figures 15 and 16. Smaller *Tb* values indicate areas of severe damage, as the parameter is positively correlated with the spatial *b*-value.

As demonstrated in Figure 15(a), the height range of the area with smaller *Tb* values extends from above the prenotch tip to a height of about 80 mm. This corresponds closely to the location of the FPZ tip monitored by DIC. Moreover, the *Tb* values reveal that the damage on the concrete side is more significant than that on the granite side, indicating greater damage severity on the concrete side when loaded up to stage P_3. When the loading continues to P_5, the *Tb* value in the interface region above the prenotch tip remains
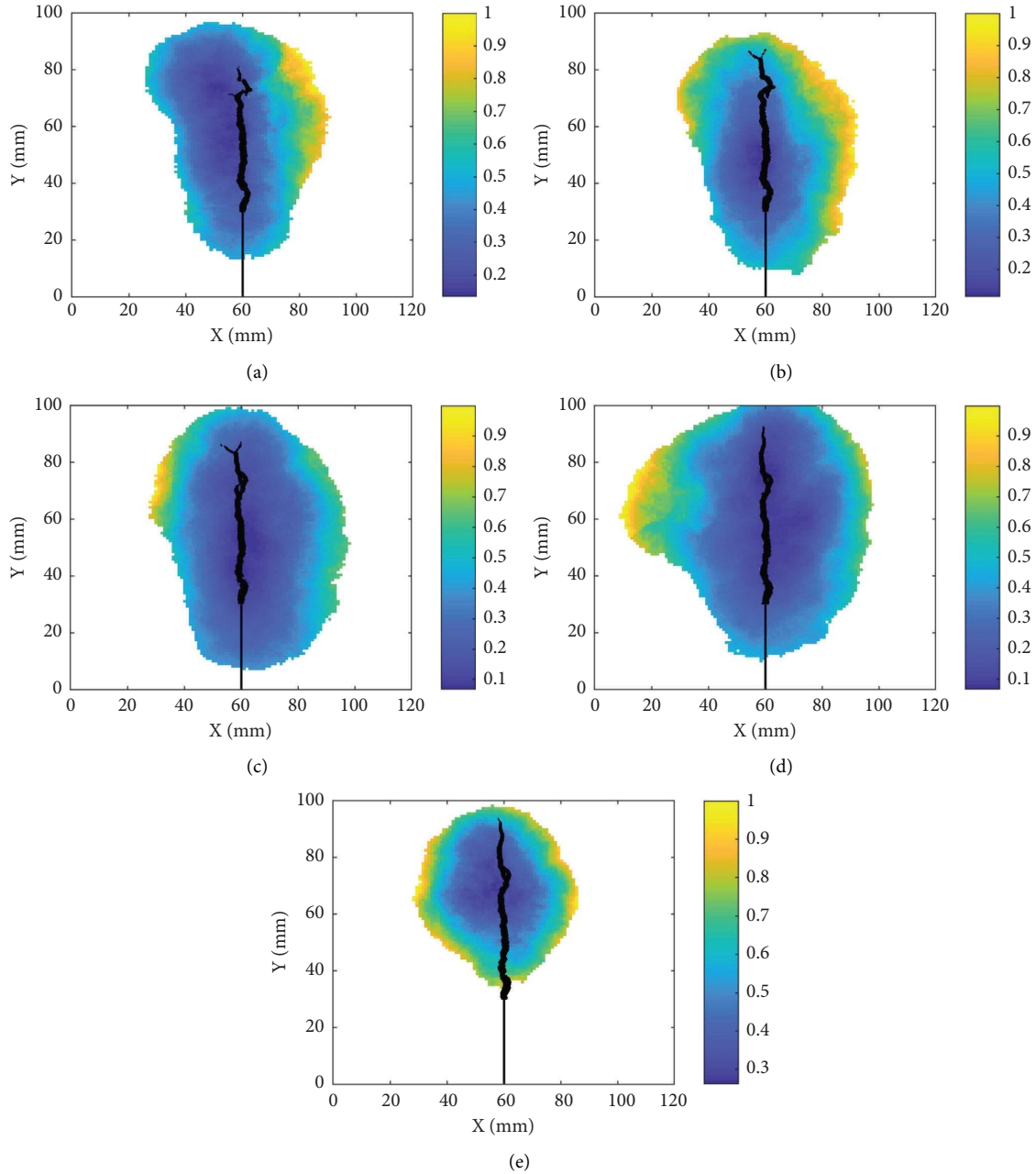
FIGURE 15: Schematic diagram of Tb of HD specimen at different loading stages. (a) $0{\sim}P_3$ stage. (b) $P_3{\sim}P_5$ stage. (c) $P_5{\sim}P_7$ stage. (d) $P_7{\sim}P_9$ stage. (e) $P_9{\sim}$end stage.

consistently low across the domain due to the continued development of the FPZ and accumulated damage at the interface. As loading proceeds, the area with smaller Tb values gradually moves upward at the shotcrete-granite interface location. Combined with the characteristics of crack extension monitored by DIC, these Tb values can be used to characterize the gradual migration of the main damage sites in the FPZ. After full development of the FPZ (Figure 15(e)), the region with smaller Tb values migrates synchronously with the movement of the end position of the FPZ, and this feature illustrates the high sensitivity of Tb values to the localization of the primary damage site.

As depicted in Figure 16(a), the crack in the shotcrete-sandstone specimen deflects directly left from the initiation point and extends into the sandstone. The Tb value is smaller on the sandstone side, and the high sensitivity of the Tb value can effectively capture significant damage on this side that is consistent with crack orientation. At stage P_5 and each subsequent stage, the area of smaller Tb values is only present on the sandstone side and corresponds closely to the expansion path of the crack. As the FPZ develops and gradually migrates upward, the area with smaller Tb values also moves upward consistently with this trend. This characteristic highlights the high consistency
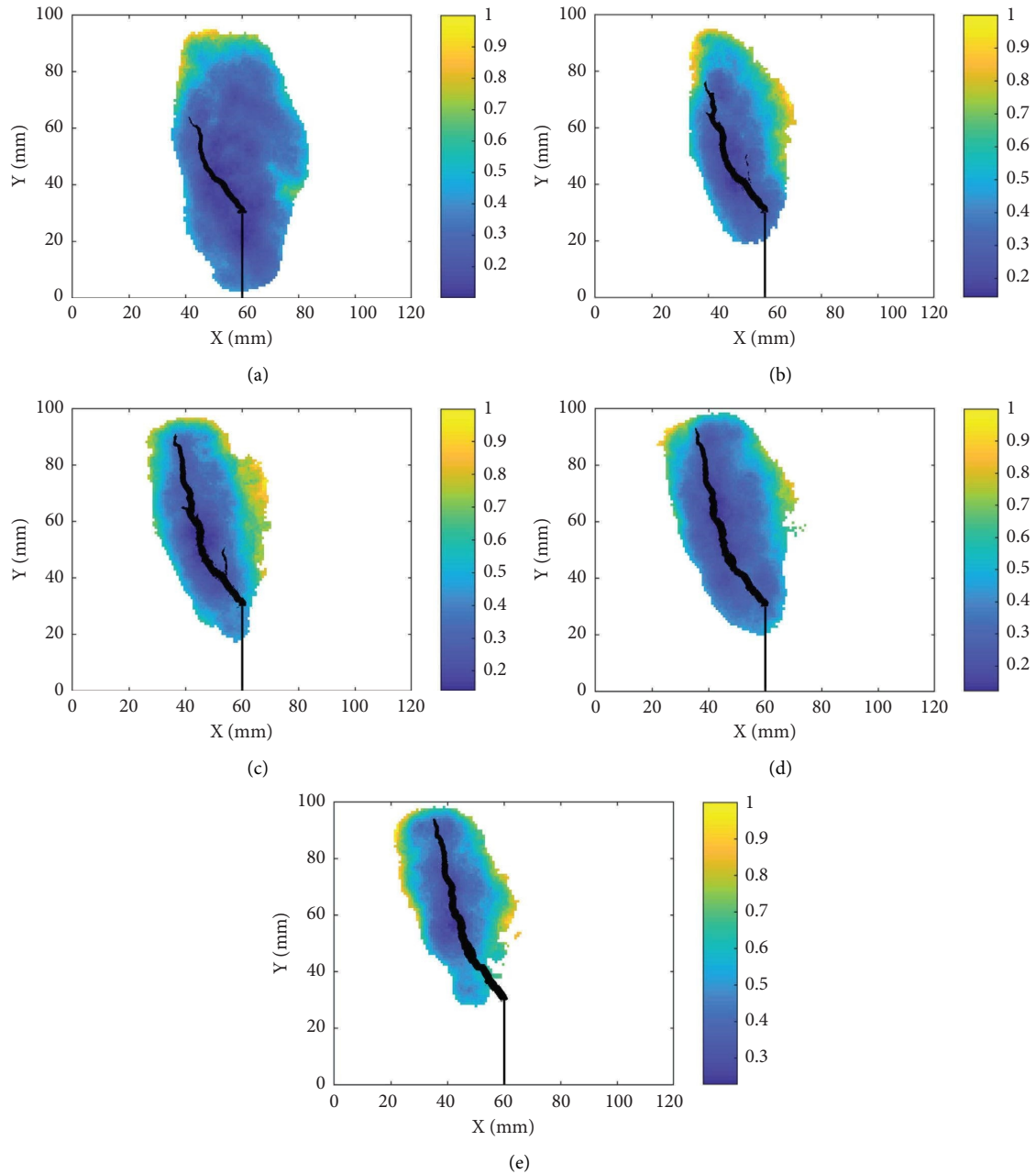
FIGURE 16: Schematic diagram of Tb of SD specimen at different loading stages. (a) $0 \sim P_3$ stage. (b) $P_3 \sim P_5$ stage. (c) $P_5 \sim P_7$ stage. (d) $P_7 \sim P_9$ stage. (e) $P_9 \sim$ end stage.

between the migration of the FPZ and the changes in the Tb values.

The above analysis demonstrates that the Tb values can provide a refined characterization of the location and severity of fracture damage in shotcrete-rock specimens, and their migration characteristics are consistent with the development pattern of the FPZ monitored by DIC. This suggests that AE can potentially be used to monitor the development pattern of the FPZ inside the shotcrete-rock specimen. It should be noted, however, that while the heat map areas of Tb agree well with the fracture extension path, they only provide a rough estimate of the FPZ development.

Therefore, it is necessary to explore different threshold values for Tb in conjunction with the dimensions of the FPZ monitored by DIC to better characterize the FPZ of shotcrete-rock specimens using the Tb parameter.

Given that the ends of the FPZ of HD and SD specimens migrate upward after stage P_9, the correspondence between the Tb values and the FPZ at different threshold values is analyzed for the P_9-end stages. The results are shown in Figures 17 and 18, respectively. The threshold value represents the rejection of Tb values greater than the threshold value, while retaining the ones below it. When the threshold value is 0.50, the tip of the HD specimen's FPZ clearly
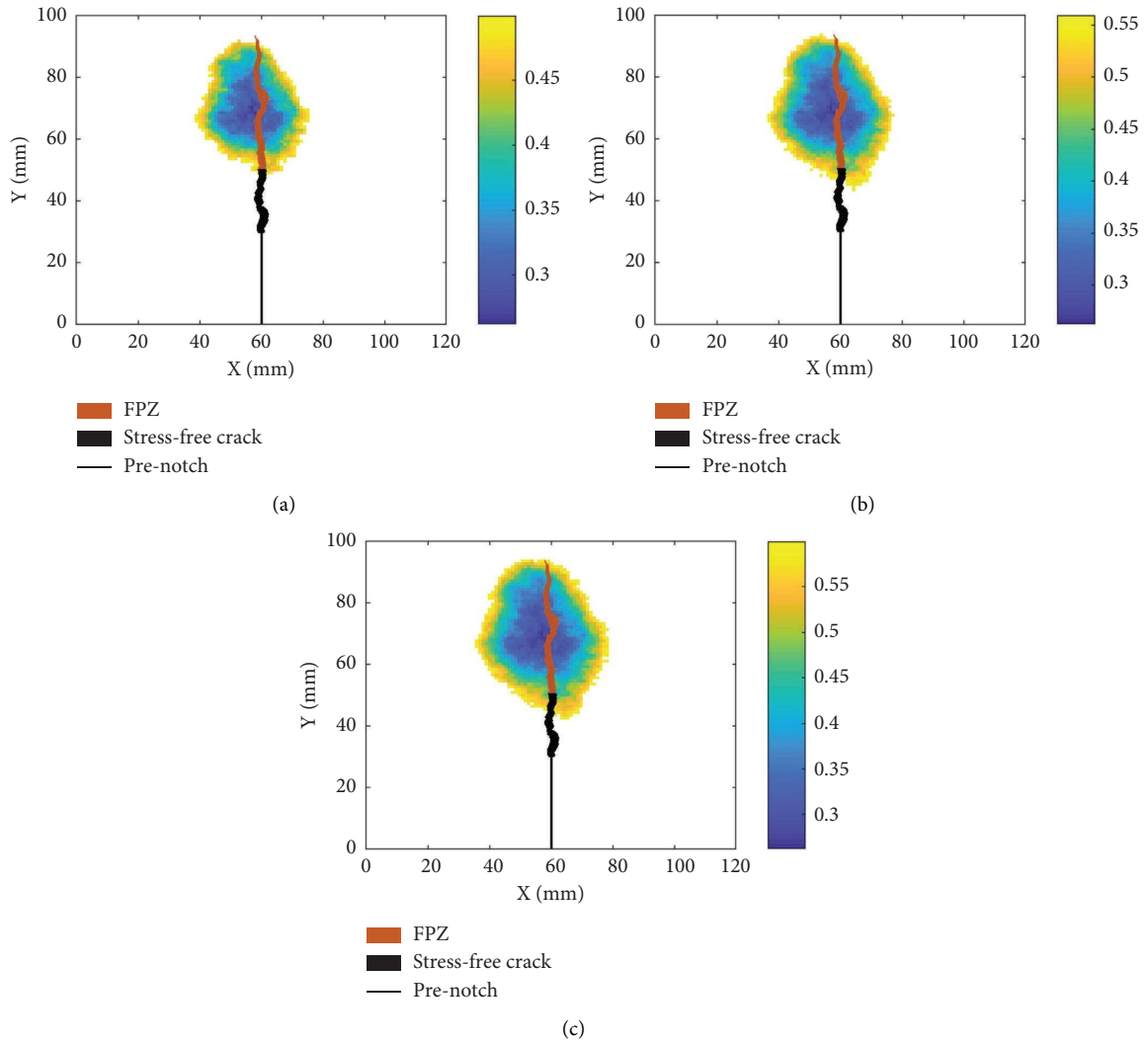
(a)

(b)

(c)

FIGURE 17: The *Tb* threshold analysis of HD specimen. (a) The *Tb* threshold: 0.50. (b) The *Tb* threshold: 0.56. (c) The *Tb* threshold: 0.60.
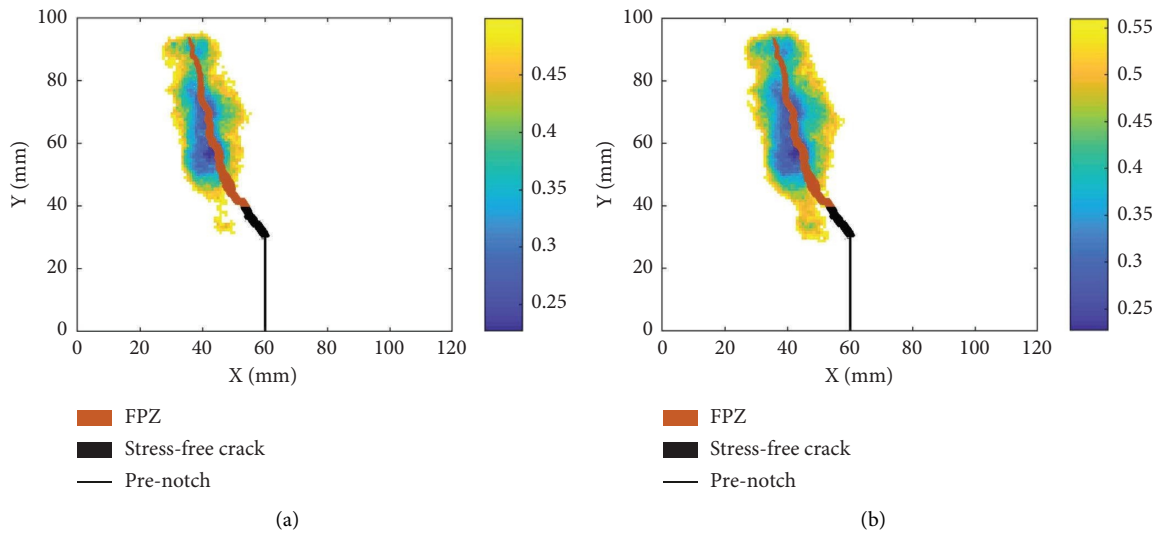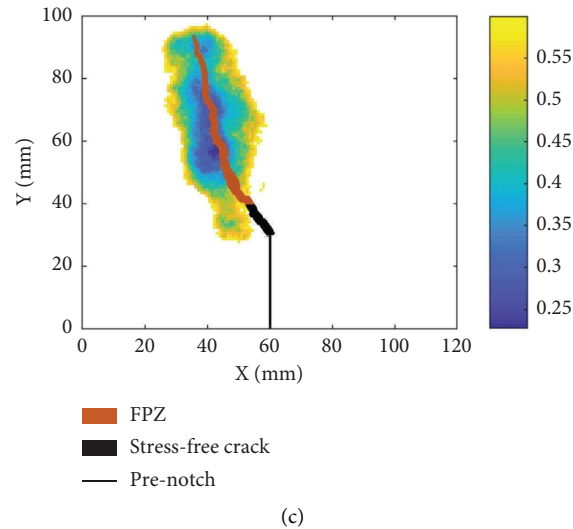

(a)

(b)

FIGURE 18: Continued.

(c)

FIGURE 18: The *Tb* threshold analysis of SD specimen. (a) The *Tb* threshold: 0.50. (b) The *Tb* threshold: 0.56. (c) The *Tb* threshold: 0.60.

exceeds the *Tb* value region, and the bottom region of the SD specimen's *Tb* value is also higher than the end of its FPZ, indicating that the threshold value of 0.50 is too small. By adjusting the threshold value from 0.60 to 0.56 to account for the degree of matching between the region of the *Tb* value and the end-tip positions of the FPZ, the *Tb* value heat map can accurately locate and characterize the size of the FPZ in granite and sandstone, showing that the influence of rock type on *Tb* values is not significant. This is important for structural safety monitoring as traditional DIC devices can only monitor surface cracks and FPZ, while *Tb* values can potentially be used to locate and measure the development of cracks and FPZ within a structure.

Although the method established in this study has been verified by using the materials in this study, whether it is suitable for the measurement of FPZ in the fracture process of other materials needs to be verified by further studies. When the specimen size or material type is different, the setting of some parameters in this method may also need to be further adjusted, which will be the focus of further research.

5. Conclusions

The study examines the FPZ properties of shotcrete-rock specimens under three-point bending loads with different interfacial roughness using DIC and AE techniques, leading to the following main findings:

(1) The lg (S_r) value is more sensitive in brittle shotcrete-granite specimens and reaches high values before peak load, with the peak value slightly increasing for rougher interfaces. Shotcrete-sandstone specimens display clear phasing characteristics at different loading stages.

(2) AE spatial *b*-value analysis enables visualization and quantification of the extent and location of damage at the shotcrete-rock interface for both types of specimens.

(3) A new parameter, *Tb*-value, is derived from AE spatial *b*-value to quantitatively characterize the FPZ. Verification through DIC suggests that the *Tb*-value can locate and quantify the size of the FPZ inside specimens.

Data Availability

The data presented in this study are available upon request from the corresponding author.

Conflicts of Interest

The authors declare that there are no conflicts of interest.

Acknowledgments

References

[1] D. F. Malan, "Manuel Rocha medal recipient simulating the time-dependent behaviour of excavations in hard rock," *Rock Mechanics and Rock Engineering*, vol. 35, no. 4, pp. 225–254, 2002.

[2] Y. Gao, Y. J. Jiang, Y. L. Du, Q. Zhang, and F. Xu, "Vibration analysis of mountain tunnel lining built with forepoling method," *Smart Structures and Systems*, vol. 21, no. 5, pp. 583–590, 2018.

[3] S. C. Yang, L. Song, Z. Li, and S. M. Huang, "Experimental investigation on fracture toughness of interface crack for rock/concrete," *International Journal of Modern Physics B*, vol. 22, no. 31, pp. 6141–6148, 2008.

[4] H. Zhong, E. T. Ooi, C. M. Song, T. Ding, G. Lin, and H. J. Li, "Experimental and numerical study of the dependency of interface fracture in concrete–rock specimens on mode

mixity," *Engineering Fracture Mechanics*, vol. 124-125, pp. 287–309, 2014.

[5] W. Dong, Z. M. Wu, and X. M. Zhou, "Fracture mechanisms of rock-concrete interface: experimental and numerical," *Journal of Engineering Mechanics*, vol. 142, no. 7, Article ID 04016040, 2016.

[6] D. W. Zhang, T. Ueda, and H. Furuuchi, "Fracture mechanisms of polymer cement mortar: concrete interfaces," *Journal of Engineering Mechanics*, vol. 139, no. 2, pp. 167–176, 2013.

[7] J. Červenka, J. M. Chandra Kishen, and V. E. Saouma, "Mixed mode fracture of cementitious bimaterial interfaces: Part II: numerical simulation," *Engineering Fracture Mechanics*, vol. 60, no. 1, pp. 95–107, 1998.

[8] D. Datta, V. Tomar, and A. H. Varma, "A path independent energy integral approach for analytical fracture strength of steel-concrete structures with an account of interface effects," *Engineering Fracture Mechanics*, vol. 204, pp. 246–267, 2018.

[9] W. Dong, D. Yang, X. Zhou, G. Kastiukas, and B. Zhang, "Experimental and numerical investigations on fracture process zone of rock–concrete interface," *Fatigue and Fracture of Engineering Materials and Structures*, vol. 40, no. 5, pp. 820–835, 2017.

[10] Z. J. Yang and X. Frank Xu, "A heterogeneous cohesive model for quasi-brittle materials considering spatially varying random fracture properties," *Computer Methods in Applied Mechanics and Engineering*, vol. 197, no. 45-48, pp. 4027–4039, 2008.

[11] D. Benarbia and M. Benguediab, "Determination of stress intensity factor in concrete material under Brazilian disc and three-point bending tests using finite element method," *Periodica Polytechnica-Mechanical Engineering*, vol. 59, no. 4, pp. 199–203, 2015.

[12] W. Dong, S. Song, B. Zhang, and D. Yang, "SIF-based fracture criterion of rock-concrete interface and its application to the prediction of cracking paths in gravity dam," *Engineering Fracture Mechanics*, vol. 221, Article ID 106686, 2019.

[13] K. Otsuka and H. Date, "Fracture process zone in concrete tension specimen," *Engineering Fracture Mechanics*, vol. 65, no. 2-3, pp. 111–131, 2000.

[14] K. Duan, X. Z. Hu, and F. H. Wittmann, "Boundary effect on concrete fracture and non-constant fracture energy distribution," *Engineering Fracture Mechanics*, vol. 70, no. 16, pp. 2257–2268, 2003.

[15] Z. M. Wu, H. Rong, J. J. Zheng, F. Xu, and W. Dong, "An experimental investigation on the FPZ properties in concrete using digital image correlation technique," *Engineering Fracture Mechanics*, vol. 78, no. 17, pp. 2978–2990, 2011.

[16] W. Dong, X. M. Zhou, and Z. M. Wu, "On fracture process zone and crack extension resistance of concrete based on initial fracture toughness," *Construction and Building Materials*, vol. 49, pp. 352–363, 2013.

[17] Q. Lin, H. Yuan, L. Biolzi, and J. F. Labuz, "Opening and mixed mode fracture processes in a quasi-brittle material via digital imaging," *Engineering Fracture Mechanics*, vol. 131, pp. 176–193, 2014.

[18] N. Zhang, A. Hedayat, H. G. Bolaños Sosa, J. Tunnah, J. J. González Cárdenas, and G. E. Salas Álvarez, "Estimation of the mode I fracture toughness and evaluations on the strain behaviors of the compacted mine tailings from full-field displacement fields via digital image correlation," *Theoretical and Applied Fracture Mechanics*, vol. 114, Article ID 103014, 2021.

[19] B. T. Huang, Q. H. Li, S. L. Xu, and C. F. Li, "Development of reinforced ultra-high toughness cementitious composite permanent formwork: experimental study and digital image correlation analysis," *Composite Structures*, vol. 180, pp. 892–903, 2017.

[20] B. Doll, H. Ozer, J. J. Rivera-Perez, I. L. Al-Qadi, and J. Lambros, "Investigation of viscoelastic fracture fields in asphalt mixtures using digital image correlation," *International Journal of Fracture*, vol. 205, no. 1, pp. 37–56, 2017.

[21] S. A. Safavizadeh and Y. R. Kim, "Fatigue and fracture characterization of fiberglass grid-reinforced beam specimens using four-point bending notched beam fatigue test and digital image correlation technique," *Materials and Structures*, vol. 50, no. 2, pp. 110–113, 2017.

[22] W. Dong, Z. Wu, X. Zhou, N. Wang, and G. Kastiukas, "An experimental study on crack propagation at rock-concrete interface using digital image correlation technique," *Engineering Fracture Mechanics*, vol. 171, pp. 50–63, 2017.

[23] Y. M. Wang, S. W. Hu, and Z. He, "Mechanical and fracture properties of geopolymer concrete with basalt fiber using digital image correlation," *Theoretical and Applied Fracture Mechanics*, vol. 112, Article ID 102909, 2021.

[24] M. Moazzami, M. R. Ayatollahi, and A. Akhavan-Safar, "Assessment of the fracture process zone in rocks using digital image correlation technique: the role of mode-mixity, size, geometry and material," *International Journal of Damage Mechanics*, vol. 29, no. 4, pp. 646–666, 2020.

[25] S. Zhang, H. Wang, X. Li, X. Zhang, D. An, and B. Yu, "Experimental study on development characteristics and size effect of rock fracture process zone," *Engineering Fracture Mechanics*, vol. 241, Article ID 107377, 2021.

[26] S. M. Aghajanzadeh and H. Mirzabozorg, "Concrete fracture process modeling by combination of extended finite element method and smeared crack approach," *Theoretical and Applied Fracture Mechanics*, vol. 101, pp. 306–319, 2019.

[27] A. M. Pakdaman, M. Moosavi, and S. Mohammadi, "Experimental and numerical investigation into the methods of determination of mode I static fracture toughness of rocks," *Theoretical and Applied Fracture Mechanics*, vol. 100, pp. 154–170, 2019.

[28] X. Hu, Q. Li, Z. Wu, and S. Yang, "Modelling fracture process zone width and length for quasi-brittle fracture of rock, concrete and ceramics," *Engineering Fracture Mechanics*, vol. 259, Article ID 108158, 2022.

[29] Y. X. Tang, H. N. Chen, and J. Z. Xiao, "Size effects on the characteristics of fracture process zone of plain concrete under three-point bending," *Construction and Building Materials*, vol. 315, Article ID 125725, 2022.

[30] M. Naderloo, M. Moosavi, and M. Ahmadi, "Using acoustic emission technique to monitor damage progress around joints in brittle materials," *Theoretical and Applied Fracture Mechanics*, vol. 104, Article ID 102368, 2019.

[31] S. N. Mat Saliah, N. Md Nor, N. Abd Rahman, S. Abdullah, and M. Subri Tahir, "Evaluation of severely damaged reinforced concrete beam repaired with epoxy injection using acoustic emission technique," *Theoretical and Applied Fracture Mechanics*, vol. 112, Article ID 102890, 2021.

[32] Q. Han, G. Yang, J. Xu, Z. Fu, G. Lacidogna, and A. Carpinteri, "Acoustic emission data analyses based on crumb rubber concrete beam bending tests," *Engineering Fracture Mechanics*, vol. 210, pp. 189–202, 2019.

[33] M. N. Noorsuhada, I. Azmi, N. M. Bunnori, M. S. Soffian Noor, M. S. Hamidah, and S. Shahiron, "Classification of damage mode of reinforced concrete beams using acoustic

emission technique. Advanced Materials Research," *Trans Tech Publications Ltd*, vol. 626, pp. 953–957, 2013.

[34] A. Nair and C. S. Cai, "Acoustic emission monitoring of bridges: review and case studies," *Engineering Structures*, vol. 32, no. 6, pp. 1704–1714, 2010.

[35] Z. H. El-Isa and D. W. Eaton, "Spatiotemporal variations in the b-value of earthquake magnitude-frequency distributions: classification and causes," *Tectonophysics*, vol. 615, pp. 1–11, 2014.

[36] Y. Guo, X. Chen, H. Yang, L. Hu, J. Zhang, and X. Fan, "Experimental study on direct tension behavior of concrete through combined digital image correlation and acoustic emission techniques," *Structural Concrete*, vol. 20, no. 6, pp. 2042–2055, 2019.

[37] T. H. W. Goebel, T. W. Becker, D. Schorlemmer et al., "Identifying fault heterogeneity through mapping spatial anomalies in acoustic emission statistics," *Journal of Geophysical Research: Solid Earth*, vol. 117, no. B3, 2012.

[38] K. Aki, "Maximum likelihood estimate of b in the formula log N= a-bM and its confidence limits," *Bull Earthq Res Inst. Tokyo Univ*, vol. 43, pp. 237–239, 1965.

[39] J. C. I. Standard, *Method of test for fracture energy of concrete by use of notched beam. JCI-S-001e2003*, Japan Concrete Institute, Tokyo Japan, 2003.

[40] D. Ren, B. Liu, S. Chen et al., "Visualization of acoustic emission monitoring of fracture process zone evolution of mortar and concrete beams under three-point bending," *Construction and Building Materials*, vol. 249, Article ID 118712, 2020.